We are IntechOpen, the world's leading publisher of Open Access books Built by scientists, for scientists

4,800
Open access books available

122,000
International authors and editors

135M
Downloads

Our authors are among the

154
Countries delivered to

TOP 1%
most cited scientists

12.2%
Contributors from top 500 universities

WEB OF SCIENCE™

Selection of our books indexed in the Book Citation Index in Web of Science™ Core Collection (BKCI)

Interested in publishing with us?
Contact book.department@intechopen.com

Numbers displayed above are based on latest data collected.
For more information visit www.intechopen.com

26

Design, Calibration and Application of a Seafloor Laser Scanner

Chau-Chang Wang[1], Da-jung Tang[2] and Todd Hefner[3]
[1]*Institute of Applied Marine Physics and Undersea Technology*
National Sun Yat-sen University
[2,3]*Applied Physics Lab, Washington University*
[1]*Taiwan*
[2,3]*USA*

1. Introduction

The surface of a seabed is influenced by wave motions, current disturbance, sediment transportation and biological activities. The scale of the features on the seabed varies from meters for large sandwaves to less than one millimeter for prints left by benthic activities. These features are important information for the sea bottom related studies. For example, marine biologists are interested in the evolution of prints on a seabed because it reveals the quantity and activity of benthos. For underwater archaeology study, accurate in-situ measurement of the site is a crucial step for the site preservation. The roughness of the seabed is one of the key parameters in modeling high-frequency underwater acoustic wave scattering. Different tools, optical-, acoustic- or electric-based, have been developed to provide measurement under different environment conditions in different scales.

Photography is a popular method used as a monitoring or surveying tool for underwater research. It provides qualitative information for archaeological site documentation and coral reef habitat monitoring (Klimley & Brown, 1983; Broadwater, 1988). However, unlike the application in the air, underwater image quality is strictly limited by illumination, range and environmental factors such as turbidity. If the target is several meters away from the camera, even under the best water conditions, photos cannot give satisfactory results. For example, Fig. 1 is a photo taken during an underwater safety inspection of pier structures. The gray area is a patch of barnacle settlement, and the dark area is a rust pot. Unless we know what we are looking at in the photo, in general the undersea world lacks references to determine the nature and the dimension of features.

An popular method called *structured light* can overcome the aforementioned problem. The idea is to project a light source with know pattern onto the scene to enhance the signal-to-noise ratio. The dimension of the feature is inferred from the distortion of the structured light in the image or from the time-of-flight of the light pulse (Myers, 1980; Rocher & Keissling, 1975; K.S. Fu & Lee, 1987). Active light source is used, so it is classified as *active vision*. Laser scanning is a typical case of active vision. They are widely used in many applications of various scales, such as terrain survey and mapping (large scale), reverse engineering and prototyping (middle scale), and microscopic-particle image velocimetry (micro scale)

Fig. 1. An sample underwater photo taken during a pier inspection.

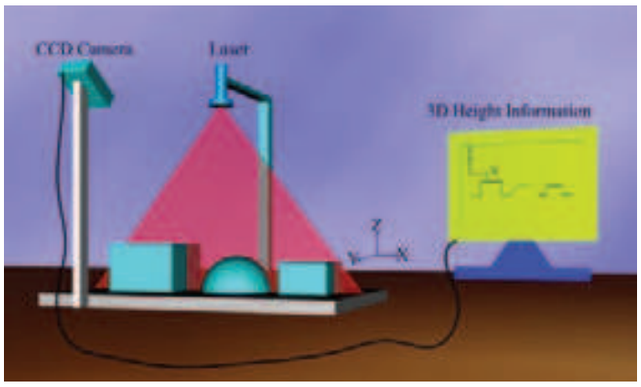

Fig. 2. Concept of structured light scanning: A laser light stripe projected on a target, and the reflection is captured by a camera to infer the dimension of the feature.

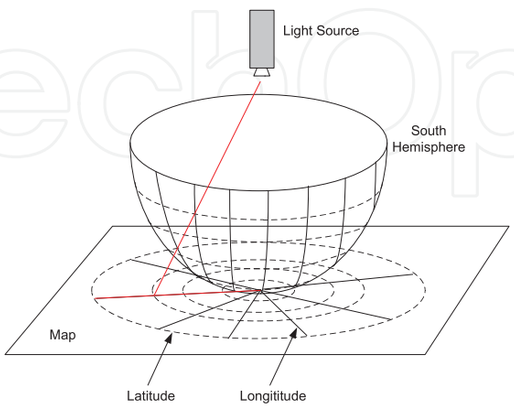

Fig. 3. Schematic of map projection: a light source projects the terrain of the earth on a plane sheet to make a map. The location of a point can be referred from the longitudes and latitudes.

(Campbell, 2006; Son & Lee, 2002; Melling, 1997; Raffel et al., 2007). As illustrated in Fig. 2, the light stripe projected on the target blocks leaves a trace on the surface which is the cross-section of the block at that location. A camera can be placed at a proper distance with an oblique perspective angle to observe the deformed light stripe. The laser stripe seen in the camera resembles the silhouette of the target. The high contrast of the laser scan line in the image can be extracted by proper thresholding. It should be noted that the offset of the laser line is not necessarily proportional to the height of the target because the camera is pointed at an oblique angle to the target such that the image generally has some distortion. Therefore a calibration is needed to convert the laser scan line described in pixel coordinates to the actual dimension of the profile (Li et al., 1989). Applying this idea in the water, Harbor Branch Oceanographic Institution installed a laser line scanning system in their Johnson-Sea-Link submersible to locate possible seafloor rock outcrops (Kocak et al., 1999; Ogawa, 2000). Crawford and Hay constructed a laser scanning system to record the seabed elevation variation and suspension events (Crawford & Hay, 1998).

To have a full 3-D measurement of the environment, the scanning head needs to be mounted on a linear track or rotating shaft to provide a third degree of freedom. As a result, for such a line scanning system, full 3D modeling of the camera is not necessary. The camera calibration can be simplified as finding a 2D-to-2D mapping, i.e. points in pixel coordinates to the coordinates on the scanning plane. Chen and Kak took this idea and simplified the optical model (Chen & Kak, 1989). They used a 4×3 transformation matrix to characterize this mapping. Theoretically, only four object points at known locations are required to determine this matrix. This method is attractive because it does not involve any low-level details of the camera and the projection light model parameters. On the other hand, a single constant transformation matrix cannot account for the nonlinear optics of the camera over the entire field of view. Another approach is to use multiple regression for relating a group of grid points on the laser scanning plane to the their images in the pixel coordinates (Gujarati, 2003). This approach is simple; however, for uneven distorted images, it is difficult to find appropriate polynomial functions to accurately characterize the nonlinearity.

In stead of tackling the camera calibration as a problem of finding intrinsic and extrinsic parameters for the camera model, we propose an empirical method in which the view seen by the camera is divided into smaller regions and local linear maps are built for each region. Ideas analogous to longitude and latitude lines of a map are adopted to refine the accuracy of laser line scanning. We utilize the properties of the structured-light-oriented geometry to simplify the process, while the desired accuracy is maintained. The goal is to develop a laser scanner to measure underwater features with millimeter resolution in general. In this chapter, (1) a map-projection-based camera calibration for structural light scanning is introduced; (2) step-by-step analyses of the measurement error bounds are presented; (3) precise point-to-point comparisons between test pieces fabricated by a CNC (computer numerical control) milling machine and the scanning results are provided to verify the efficacy of our approach; (4) a roughness-known model surface is scanned to decide the reliable roughness spectrum measurement bounds of the scanner; (5) field experiments at water depth of eighty meters are reported.

2. Plane-based camera calibration

Before explaining the calibration method, let us first review the concept of map projection. Consider a transparent hemisphere painted with longitude and latitude lines on its surface

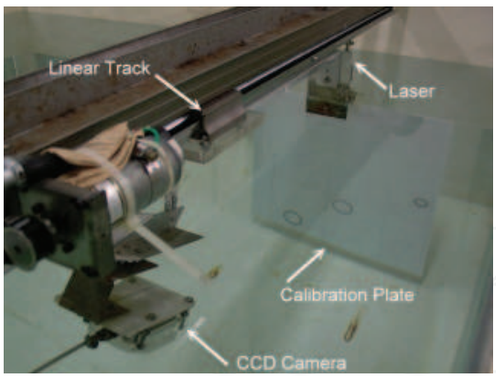

Fig. 4. Experimental Setup.

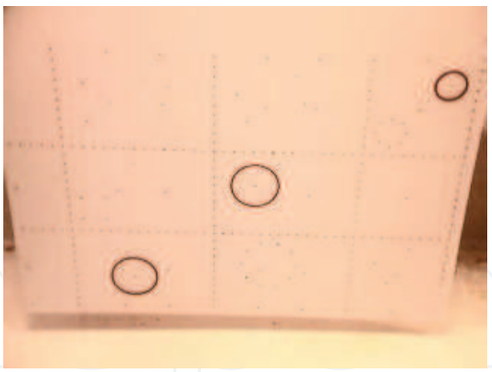

Fig. 5. The calibration board seen from the CCD camera.

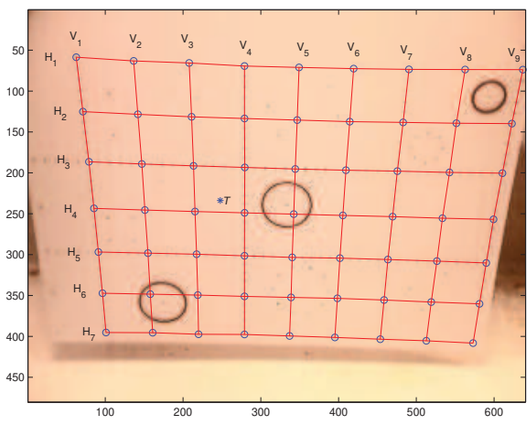

Fig. 6. Longitude and latitude lines created by curve-fitting the grid dots.

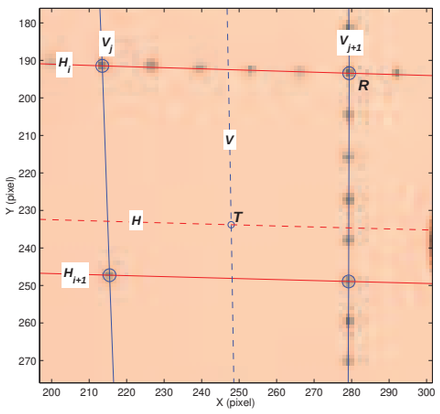

Fig. 7. Close-up of a target point T on the calibration board.

as shown in Fig. 3. To make a map, we put a light source at the top of the hemisphere and a screen tangent to the south pole. The light rays project the terrain and the longitude and latitude lines onto the screen to create the map. The longitude and latitude lines serve as references to relate a point on the map with its location on the hemisphere. For a location which is not right at the intersection of a longitude line and a latitude line, we can estimate its coordinates from its distances to the neighboring longitude/latitude lines. Bearing this idea in mind, the camera calibration for measuring features on a plane can be analogized to the projection problem: replace the projection screen with a camera, and the transparent hemisphere with a board with known graticules placed coplanarly with the measurement plane. To decide the coordinates of a point in the image is like reading a map to find out the coordinates of a town.

For our calibration setup, a laser line source and a camera were fixed on a linear stage and submerged into water (as shown in Fig. 4). Grid points, drilled with 50 mm separation by a CNC milling machine, are laid on an acrylic board as shown in Fig. 5. This board, called the *calibration board* hereafter, is carefully aligned with the plane of the laser scanning sheet. In order to cover a larger view, a camera with a wide-angle lens is placed roughly one meter away from the board. The optical axis of the camera is pointed downward approximately 30° from the horizon. The points seen in the camera are shown in Fig. 5. It is obvious that the upper half of the image is larger than the lower half. The formations of the grid points are not

straight and parallel lines but curvilinear near the boundary of the image frame. However, this distortion is mild and varies smoothly from the center to the sides. We curve-fit the grid points to create longitude lines, V_j, and latitude lines, H_i, as shown in Fig. 6, such that the scope is divided into smaller quadrangular regions. Within a quadrangle, we can assume that the distortion of the image is smooth and linear. Therefore, given a target point, T, shown in Fig. 6 or the close-up in Fig. 7, its location on the calibration board can be estimated from the distances (in pixels) between itself and its four neighboring sides V_j, V_{j+1}, H_i and H_{i+1}. A rough estimate of T is approximately one half of a spacing from V_j and three quarters of a spacing from H_i. In other words, its location is roughly 25 mm right from the longitude line V_j and 37.5 mm beneath the latitude line H_i. Since the grid points were laid with 50 mm spacing, the coordinates of T can be inferred from the closest known point, e.g. R. For example, if R's coordinates are (100 mm, 250 mm) in the calibration board coordinate system, T will be around (125 mm, 212.5 mm).

In stead of *estimation*, $T's$ position can be obtained with respect to a corner of the quadrangle with following procedures. Interpolate from the surrounding longitude and latitude lines a set of vertical and horizontal lines which intersect at the target point[1]. For the example we can have a linear combination of H_i and H_{i+1} with some proper weightings to construct a horizontal line H which passes through T as

$$H = w_i H_i + w_{i+1} H_{i+1}, \tag{1}$$

where w_i, $w_{i+1} \geq 0$ and $w_i + w_{i+1} = 1$. If the weighting factors ratio is $w_i : w_{i+1} = 0.26 : 0.74$, we find that T is 50 mm$\times$0.74 =37 mm beneath H_i , or 50 mm$\times$0.26 =13 mm above H_{i+1}. The horizontal component can be obtained likewise.

In summary, this method does not explicitly involve any intrinsic or extrinsic parameters of the camera or the relative position of the laser scanning sheet. All non-linearities are lumped together and linearized separately for each quadrangle in the map. Therefore when a laser scanning sheet is projected on the target, the relative position of the laser line segment in the calibration board coordinate system can be calculated with the same idea. In the following section, we will present the procedures of constructing such a projection map for the laser scanning system.

3. Implementation

First of all, we define the following terms used in explaining the calibration and measurement procedures.

A Control Points

Grid dots with 50 mm separation, called control points, are laid on the surface of an acrylic board as shown in Fig. 5. These dots were drilled with a CNC milling machine, so their positions are assumed to be accurate to the CNC machine accuracy which is 0.01 mm for our case. Each dot is of finite size, and its intensity-weight center is used as its nominal location. As shown in Fig. 8, the distances between control points in the image are not fixed but varying mildly from point to point. An algorithm was developed to search for the control points adaptively. As a first step, we manually select the upper-left dot (bounded in

[1] With the functional forms of the neighboring longitude lines and latitude lines, we can use bisection to decide a set of vertical and horizontal lines which intersect at the target point.

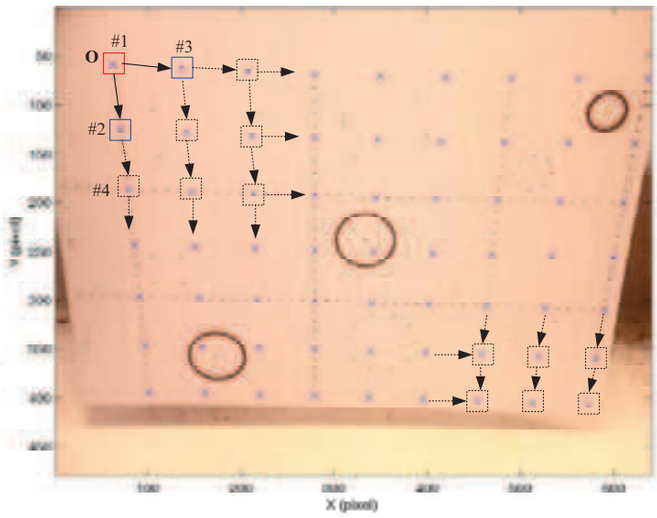

Fig. 8. The idea of adaptive searching for control points on the calibration board.

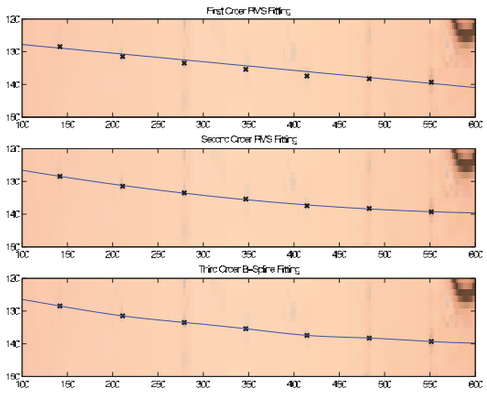

Fig. 9. Comparison of different fitting methods for grid points.

box #1), and the dot beneath (bounded in box #2) and right next to it (bounded in box #3). We use the displacement vector from dot #1 to #2 as a reference to estimate the approximate location of the control point beneath #2 (denoted as #4). A bounding box is placed at the tip of the displacement vector to search for the dot. Once dot #4 is found, a new displacement vector from #2 to #4 can be used to search downward further. In the same manner, we can search toward the right-hand side. This process is repeated until all the control points are located. We mark all the control points found with an "$\times$" as shown in Fig. 8. The control point at the upper left corner labeled as "O" is selected as the origin of the calibration board coordinate system.

B Longitude and Latitude Lines

All the control points are laid with equal spacing on the board. Therefore the trend of the local image distortion is characterized by the relative displacement of the control points and the overall distortion can be characterized by the longitude and latitude lines which are obtained by curve-fitting the control points (in pixel coordinates). To achieve better fitting results, the latitude lines are described as $Y = Y(X)$, while the longitude lines are described as $X = X(Y)$. In Fig. 9, we show the image of horizontal control points overlaid with curves obtained by three different fitting functions. From top to bottom, they are first

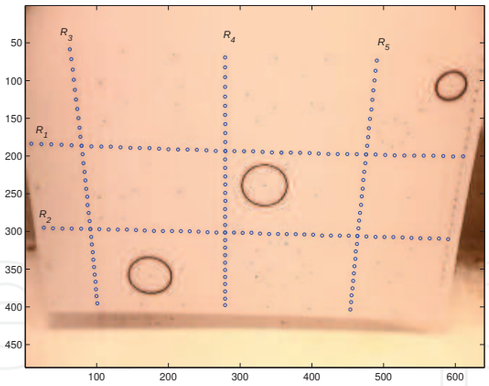

Fig. 10. Five auxiliary rulers on the calibration board.

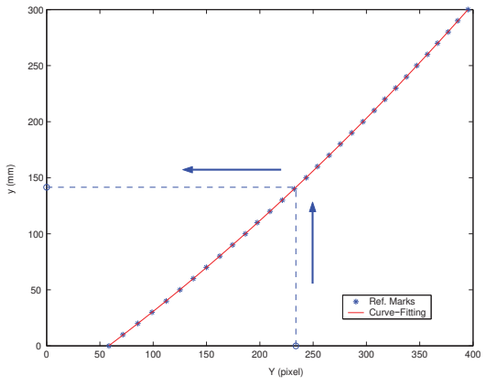

Fig. 11. Pixel coordinate of reference marks versus their calibration board coordinate for ruler R_4.

order RMS (Root Mean Square), second order RMS and cubic B-spline. In the case of first order RMS, the straight line can only pass through the neighborhood of control points, not right through them. As for second order RMS, the polynomial curve does not pass through the control points either, but it traces the control points closely. Mathematically, cubic B-spline curve is forced to pass all the control points. Because these lines are used as bases to determine the location of a target point, the correctness of the curve fit for the control points strongly influences the accuracy of the measurement. According to our analysis, the second order RMS gives the most stable performance which is a property preferred by most measurement systems (Wang & Cheng, 2007).

C Auxiliary Rulers

The longitude and latitude lines give us a rough idea of the location of a target point. The overall accuracy of the system can improved by adding denser control points on the calibration board. However, doing so would give us a crowded and confusing image. An alternative is to place marks of smaller spacing at selected locations for reference. For example, in Fig. 10 we place reference marks of 10 mm spacing on the calibration board labeled as R_1 to R_5. We give these lines another name, the *auxiliary rulers*. By the name *ruler* we mean that these reference lines help us to estimate where the actual coordinates are in a more accurate manner because the uncertainty is reduced from 50 mm to 10 mm.

We show again the closeup of T in Fig. 7. The interpolated latitude line H intersects with the closest vertical auxiliary ruler R_4 at T_4. T and T_4 are share the same y coordinate which

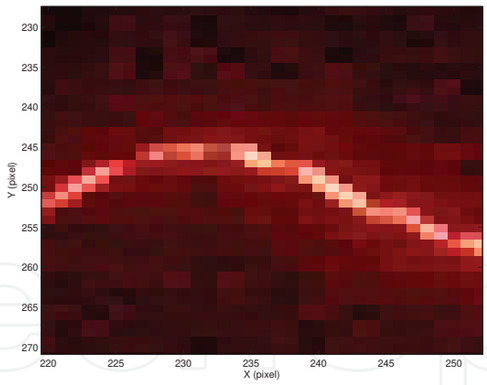

Fig. 12. A close-up image of a laser scan line casting on a sand ripple. It is obvious that the width of the laser line is more than one pixel.

can be obtained by interpolating between the two closest bounding reference marks on R_4. In Fig. 11, we plot the vertical pixel coordinate Y of each reference mark on R_4 versus the corresponding vertical coordinate y on the calibration board in millimeter. With this plot, the vertical component of T_4 in pixels is then used to look up its corresponding y coordinate in millimeter on the laser scanning plane. For example, according to Fig. 11, T_4's Y is 234.5 pixels which is converted to 142.3 mm. Likewise, T_1, the intersection of V with the near-by horizontal auxiliary ruler R_1, provides the x coordinate of T in millimeter.
We summarize the procedures as the following steps:

1 Choose two longitude lines and two latitude lines which surround the target point.

2 Iterate the weights (between one and zero) of the latitude lines until an interpolated curve passes through the target point.

3 Find the intersection of the interpolated latitude line with the closest vertical auxiliary ruler.

4 Substitute the vertical component of the coordinated in pixels found in step 3 into the ruler conversion curve to obtain the y coordinate of the point.

5 Repeat steps 2, 3 and 4 for the horizontal component.

4. Performance tests

The performance of the system depends on the longitude and latitude lines characterization, and also the effectiveness of the laser scan line image processing. Ideally, we would like to have a laser line as narrow as possible (one pixel) in width to reduce the uncertainty[2]. In reality, the scan line is several pixels wide (see the bright area in Fig. 12). In other words, depending on how we choose the location of the center of the scan line, the result might be off by a couple of pixels. From the look-up curve shown in Fig. 11 we know that a pixel in the image frame is roughly equivalent to one millimeter in linear dimension on the calibration board. This ambiguity contributes to the error in the measurement. To understand the nature of these errors, it is necessary to carry out separate experiments to identify the source of the error and its extent of influence.

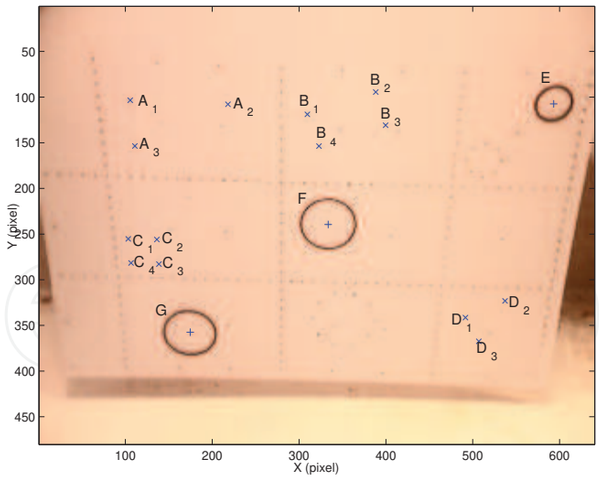

Fig. 13. Features on the calibration board for verification.

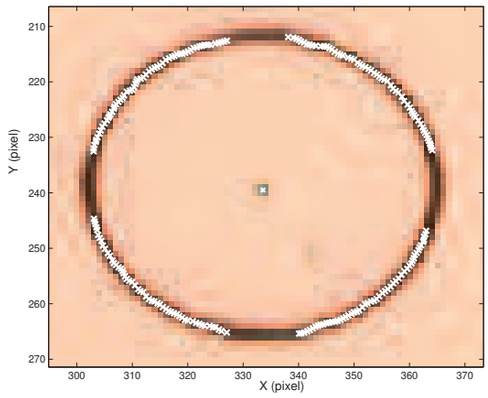

Fig. 14. Manually selected points (denoted as $\times$) on the circumference for estimating the diameter of circle E.

4.1 On-board verification

When making the calibration board, in addition to the control points and the auxiliary rulers, we also made several dots and shapes with known location and dimension. Measurement of the distance between two dots or the diameter of circles can be used to verify that the curve-fitting achieves the required accuracy.

A Point to Point Distance

There are several dots on the board, labeled as A_1 to A_4, B_1 to B_4, C_1 to C_4, and D_1 to D_4 in Fig. 13. We use the distance between points to estimate the error in our measurement. Because our approach is a point-based measurement, we expect to see that the absolute error remains bounded while the relative error tends to get smaller as the distance (denominator) increases. These results are summarized in Table 1.

B Diameter of Circles

Three circles, labeled as E, F and G, are laid at the upper, middle and lower part of the board. The circles are milled with a ϕ 0.8 end cutter and filled with the same black clay

[2] One-pixel width also poses problems if we want to have sub-pixel resolution.

Features	A_1A_2(80.00mm)			A_2A_3(89.44mm)			A_3A_1(40.00mm)		
Fitting Method	Measured	Err.	%	Measured	Err.	%	Measured	Err.	%
1st RMS	80.19	0.19	0.24	89.68	0.24	0.27	39.66	-0.34	-0.86
2nd RMS	80.01	0.01	0.01	89.43	-0.02	-0.02	39.84	-0.16	-0.39
Cubic B-Spline	86.82	5.82	7.28	94.73	5.28	5.91	40.10	0.10	0.26
Features	B_1B_2(60.00mm)			B_2B_3(30.00mm)			B_3B_4(60.00mm)		
Fitting Method	Measured	Err.	%	Measured	Err.	%	Measured	Err.	%
1st RMS	59.86	-0.14	-0.24	29.69	-0.31	-1.02	59.85	-0.15	-0.26
2nd RMS	59.80	-0.20	-0.33	29.90	-0.11	-0.35	59.84	-0.16	-0.27
Cubic B-Spline	63.77	3.77	6.28	30.03	0.03	0.09	63.89	3.89	6.48
Features	B_4B_1(30.00mm)			C_1C_2(25.00mm)			C_2C_3(25.00mm)		
Fitting Method	Measured	Err.	%	Measured	Err.	%	Measured	Err.	%
1st RMS	29.90	-0.10	-0.35	24.88	-0.12	-0.47	24.94	-0.06	-0.23
2nd RMS	29.88	-0.12	-0.39	24.91	-0.09	-0.37	25.09	0.09	0.35
Cubic B-Spline	30.16	0.16	0.55	25.62	0.62	2.49	25.09	0.09	0.37
Features	C_3C_4(25.00mm)			C_4C_1(25.00mm)			D_1D_2(40.00mm)		
Fitting Method	Measured	Err.	%	Measured	Err.	%	Measured	Err.	%
1st RMS	24.91	-0.09	-0.34	24.89	-0.11	-0.44	39.64	-0.36	-0.91
2nd RMS	24.91	-0.09	-0.34	24.95	-0.05	-0.20	39.82	-0.18	-0.46
Cubic B-Spline	25.58	0.58	2.33	24.90	-0.10	-0.42	40.45	0.45	1.13
Features	D_2D_3(50.00mm)			D_3D_1(30.00mm)					
Fitting Method	Measured	Err.	%	Measured	Err.	%			
1st RMS	49.66	-0.34	-0.68	30.45	0.45	1.51			
2nd RMS	49.72	-0.28	-0.57	30.11	0.11	0.38			
Cubic B-Spline	49.71	-0.29	-0.58	30.28	0.28	0.95			

Table 1. Distance measurement between known points. (The number in the parentheses is the nominal dimension given to the CNC milling machine.)

Features	E(28.40mm)			F(49.20mm)		
Fitting Method	Measure	Err.	Err.(%)	Measure	Err.	Err.(%)
1st RMS	28.39	-0.01	-0.04	49.04	-0.16	-0.32
2nd RMS	28.22	-0.18	-0.64	49.09	-0.11	-0.22
Cubic Spline	29.17	0.77	2.70	50.39	1.19	2.42
Features	G(49.20mm)					
Fitting Method	Measure	Err.	Err.(%)			
1st RMS	49.04	-0.16	-0.32			
2nd RMS	49.07	-0.13	-0.26			
Cubic Spline	49.63	0.43	0.88			

Table 2. Results of on-plane circles measurements. (The number in the parentheses is the nominal diameter of the circles.)

as used for control points. To obtain the diameter of the circle, we enlarge the image and manually pick out points on the circumference as shown in Fig. 14. These points are used to best-fit a circle. The diameters obtained for the circles are listed in Table 2. The results are accurate and are all well under one percent except for some measurements converted with cubic B-spline fitted longitude/latitude lines.

Here the error is defined as the measurement minus the nominal dimension, i.e. the value given to the CNC milling machine. Overall, first order and second order RMS curve-fitting give good measurement results. Almost all the relative errors of the measurement are less than 1% and the second order result is better than that of first order. Surprisingly, the cubic

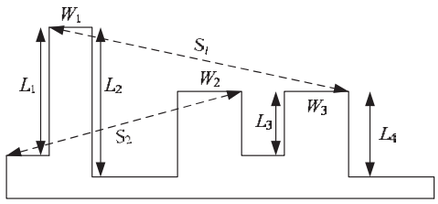

Fig. 15. The Dimensions of the grooved surface test piece.

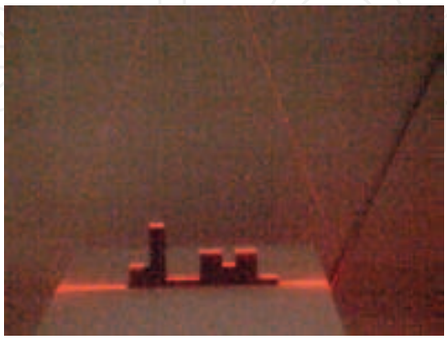

Fig. 16. A snap shot of the grooved surface test piece scanning.

B-Spline curve-fitting does not perform well; its performance fluctuates. It ranges from 0.09% for $\overline{B_2B_3}$ to 7.28% for $\overline{A_1A_2}$. This performance fluctuation results from the sensitive behavior of B-Spline fitting with respect to the minor difference of control points (Wang & Cheng, 2007). For the following experiments, only second order RMS is used to fit the longitude/latitude lines.

4.2 Grooved surface

The preceding experiments address the performance of the optical calibration alone. The final measurement result also depends on the reflection of the laser line from the target. For example a mirror-like surface may reflect the incoming beam perfectly. If the camera is not pointing along the path of the reflection, it will not see the laser profile at all. Therefore the texture of the target is a crucial factor. To determine whether the calibration remains accurate for an actual surface, we use a CNC milling machine to make a test piece which has grooves of different widths and heights as shown in Fig. 15. The laser profile seen from the CCD camera consists of line segments as shown in Fig. 16. The discontinuity of the segment is the location where the height changes. We measure the widths, the heights and the distances between edges and compare them with the nominal dimension. For this experiment, the widths are defined by the end points of the laser segments. To determine the height, we cannot treat it as the distance between the edge of a top and the corner of a groove because the corner at the bottom of a groove is a shadow zone where the laser cannot reach. Alternatively we fit the points of the laser segment with a straight line and infer the height from the distance between the two lines. We find that the absolute errors, summarized in Table 3, are all less than 0.6 mm. The measurement is accurate to 1% of the length of the features if the dimension is larger than 20 mm.

4.3 Sandwave

One major goal is to use the system to measure the roughness of a seafloor. To simulate a sandwave, we use a CNC milling machine to create a 3D surface defined by the following

Features	W_1(19.96mm)			W_2(29.96mm)			W_3(29.96mm)		
Fitting Method	Measured	Err.	%	Measured	Err.	%	Measured	Err.	%
2nd RMS	20.03	0.07	0.34	29.76	-0.20	-0.67	30.12	0.16	0.53
Features	H_1(60.00mm)			H_2(80.06mm)			H_3(20.04mm)		
Fitting Method	Measured	Err.	%	Measured	Err.	%	Measured	Err.	%
2nd RMS	59.45	-0.55	-0.91	79.40	-0.66	-0.83	19.97	-0.07	-0.36
Features	H_4(40.02mm)			S_1(154.96mm)			S_2(131.04mm)		
Fitting Method	Measured	Err.	%	Measured	Err.	%	Measured	Err.	%
2nd RMS	39.67	-0.35	-0.89	154.56	-0.40	-0.26	130.73	-0.31	-0.24

Table 3. Measurement of the grooved surface. (The numbers in the parenthesis are the dimensions measured with a caliper.)

equation:

$$z(x,y) = (A + By)\sin(Cx + D\sin(Ey)), \tag{2}$$

where x, y and z are all in millimeters and A, B, C, D and E are constants. There are two sine functions in this equation. The first one varies on the yz plane that creates ripples while the second one, appearing in the argument of the first, undulates the ripples along the y direction. The value of A determines the mean elevation of the surface, B decides how fast the amplitude of the ripple increases along the y axis, C controls the wavelength of the ripples, and D and E defines the undulating amplitude and frequency respectively. The constants are chosen such that four ripples were accommodated in a 210 mm $\times$ 210 mm $\times$ 40 mm block[3]. The ripples meander and change direction twice in the model while the amplitude increases linearly along the y direction from 1.5 mm to 8 mm. To simulate the granular texture of the seabed, a thin layer sea sand is attached to the test piece surface with adhesive. With this model, we can determine the lower limit of the amplitude which the system can detect. The CAD model and the workpiece is shown in Fig. 17 and 18 respectively.

A linear track carries the scanning head, moving at 0.5mm increments, to profile the sandwave workpiece. Altogether 400 images like the one shown in Fig. 19 are captured and processed to reconstruct the surface of the sandwave shown in Fig. 20. We plot all the data points and find that even the smallest amplitude (1.5 mm) of the sine wave is still visible on the plot. However the wave form is tilted because the base-plane of the test piece is not aligned with the xy plane of the scanning head. Several rotations and translations are carried out to align dataset with CAD model such that quantitative comparison can be done (Wang & Cheng, 2007).

We use the interpolated values of the calibrated scanning data at given locations for comparison. Four transects denoted as S_1, S_2, S_3 and S_D in Fig. 21 are selected for analysis. These locations are selected to verify the accuracy of measuring different amplitudes. The amplitude of the sine wave decreases from 7.5 mm for S_3, to 2 mm for S_1. S_D is even more challenging because it goes through different amplitudes, and it also indicates whether the phase shift between different ripples is captured correctly. The results are presented in Fig. 22 to Fig. 25. From the results we find that most of the errors are bounded between -1 mm to 1.5 mm except for the upper-left segment of the slice S_D. With this spatial resolution and accuracy, conservatively speaking, the laser scanning system should be able provide interface roughness information needed for modeling acoustic bottom interaction for 100 kHz (wavelength 15 mm) or lower.

[3] $A = 1.5$, $B = 0.043$, $C = 0.167$, $D = 2.0$ and $E = 0.042$.

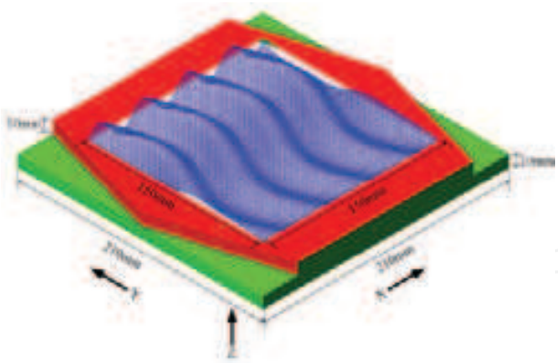

Fig. 17. The CAD model of the sandwave surface.

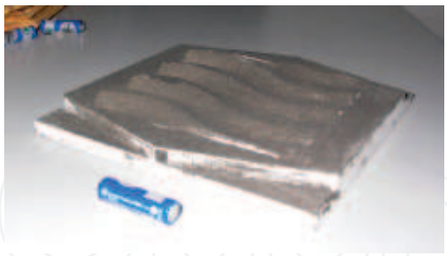

Fig. 18. The CNC machined workpiece of the simulated sandwave.

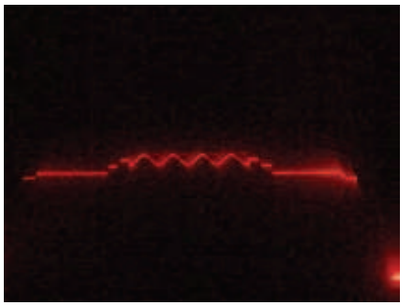

Fig. 19. A sample image of the sandwave scanning.

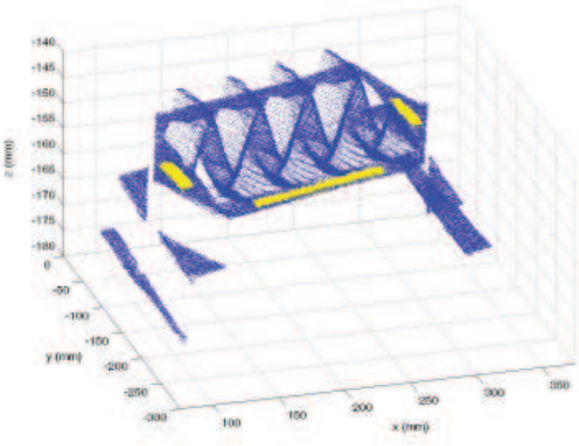

Fig. 20. The raw data of the sandwave scanned.

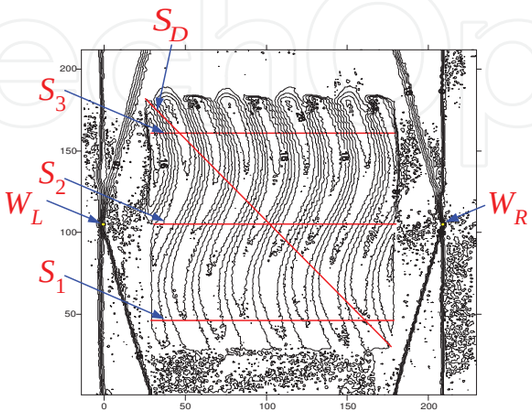

Fig. 21. The contour plot of the sandwave surface. (After rotation, translation and yawing calibration)

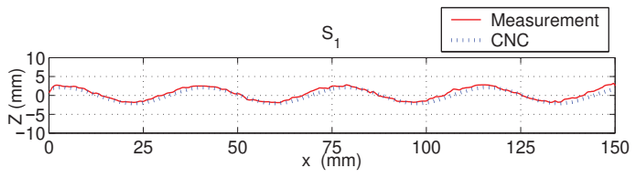

Fig. 22. Measurements (solid curves) v.s. CAD model theoretical values (dotted curves) at S_1 on the CNC machined workpiece of the simulated sandwave.

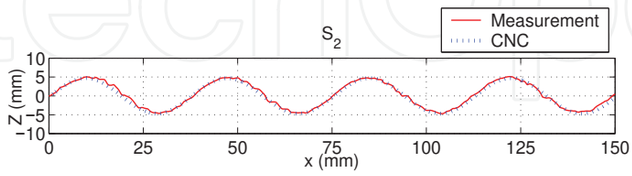

Fig. 23. Measurements (solid curves) v.s. CAD model theoretical values (dotted curves) at S_2 on the CNC machined workpiece of the simulated sandwave.

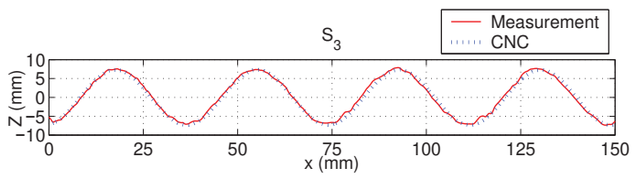

Fig. 24. Measurements (solid curves) v.s. CAD model theoretical values (dotted curves) at S_3 on the CNC machined workpiece of the simulated sandwave.

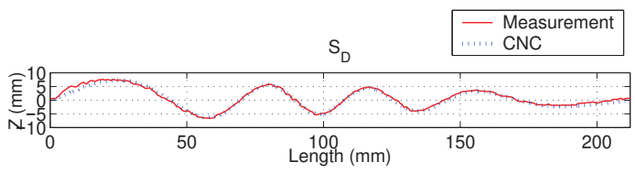

Fig. 25. Measurements (solid curves) v.s. CAD model theoretical values (dotted curves) at S_D on the CNC machined workpiece of the simulated sandwave.

5. Rough surface measurement

For studying high-frequency acoustic scattering, the most important input is the roughness power spectrum of the interface in the frequency band of interest (Williams et al., 2004). A proper estimation of the errors in this spectrum is essential for the validation and application of acoustic scattering models. It is necessary to establish a procedure to quantitatively assess the performance of the proposed laser scanner when measuring bottom interface roughness. However, conventionally, laser scanning performance assessment usually uses objects which are smooth and regular in shape. These test objects tend not to reflect the variation in surface height typically observed on sediment interfaces. The error bound obtained with these test objects is not sufficient to infer the system performance in measuring actual sediment roughness or the statistics of the roughness. In order to establish a subjective assessment of the scanner's performance in acquiring roughness spectrum, a model-realistic surface

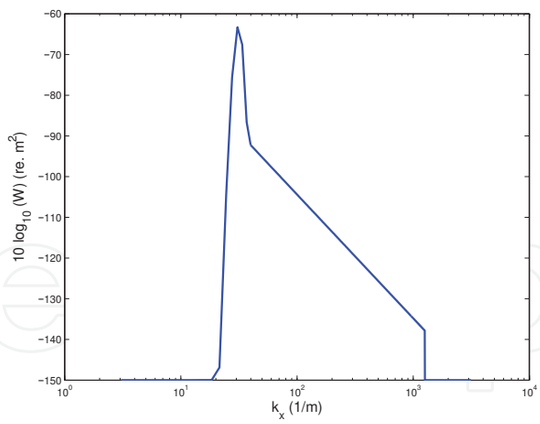

Fig. 26. Slice of the two-dimensional power spectrum along the positive k_x-axis. The spectrum has a Gaussian anisotropic (ripple) component and an isotropic power-law component.

was developed. Creating a realistic rough surface with known topography is challenging and is rarely done. With CNC milling machines, several researchers have constructed rough surfaces for use in studying the scattering of acoustic (Mellema, 1999; Summers et al., 2005) and electromagnetic waves (Kuga & Phu, 1996) from rough surfaces. These surfaces typically implement an isotropic roughness with a power-law spectrum and a surface size that is compatible with the acoustic or electromagnetic wavelength of interest. The surface topography we chose was to reflect the isotropic roughness and the anisotropic surface ripple observed during the high-frequency Sediment Acoustics Experiment (SAX99) (Thorsos et al., 2001; Briggs et al., 2004).

5.1 Power spectrum of the model surface

Certain ripple fields in near shore waters have the following properties: When the ripples are absent, the bottom roughness can be adequately described by an isotropic power-law power spectrum (Briggs, 1989) and when ripples are present, the bottom roughness can be considered as a superposition of an isotropic power-law component and a ripple component (Thorsos et al., 2000). To represent a realistic sediment interface, the design of the model surface was based on the SAX99 power spectrum and is composed of the two spectral components, $W = W_g + W_p$, where W_g is the shifted Gaussian power spectrum component, which generates ripples, and W_p is the isotropic power-law component.
The Gaussian power spectrum, W_g is expressed as

$$W_g = \frac{h^2}{4\pi\sigma^2}\left[\exp\left(-\frac{(k_x-k_0)^2+k_y^2}{2\sigma^2}\right)+\exp\left(-\frac{(k_x+k_0)^2+k_y^2}{2\sigma^2}\right)\right] \tag{3}$$

where (k_x,k_y) is the horizontal wave vector, h is the RMS height, $k_0 = 2\pi/\lambda_0$ is the center wavenumber with λ_0 being the dominant ripple wavelength, and σ determines the spread of the dominant ripple component. To make the size of the model surface manageable, we scaled the ripple size measured during SAX99 by a factor of 2/5, which applied to both the ripple wavelength and the ripple height. This choice ensures that shadowing during optical measurements behind ripples is the same for the field and model scenarios. As a result, the following set of parameters were used for the Gaussian spectrum: $h = 0.005$ m, $\lambda_0 = 0.2$ m, and $\sigma = 0.05$ m^{-1}. This spectrum produces ripples running predominantly along the x-axis.

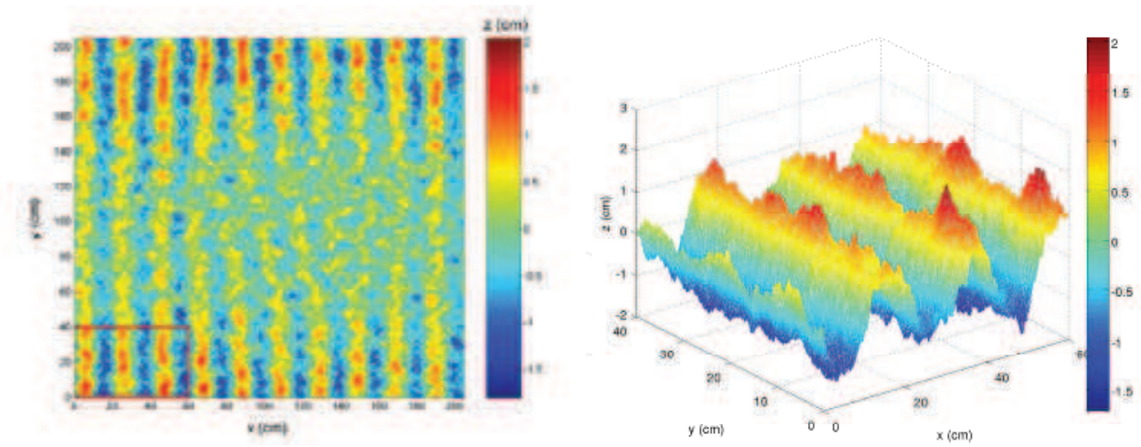

(a) (b)

Fig. 27. (a) The realization of the rough surface over a 200 × 200 cm^2 area. A smaller portion of this surface, a 40 × 60 cm^2 section on the lower left corner, was used for machining. (b) Magnification of the 40 × 60 cm^2 section used for the sample seafloor.

The isotropic portion of the power spectrum, W_p is written as a truncated power-law

$$W_p = \begin{cases} \frac{w_2}{k_r^{\gamma_2}}, & (k_1 \leq k_r \leq k_2) \\ -150 \text{ dB, otherwise} \end{cases} \tag{4}$$

where $k_r = \sqrt{k_x^2 + k_y^2}$, w_2 is the spectral strength, k_2 is the fine-scale or high-wavenumber cutoff, k_1 is the large-scale or low-wavenumber cutoff, which occurs just before the onset of the ripple component to make the observed ripples dominant at large scales. For this component, $k_1 = 1.1k_0$, $k_2 = 2\pi/0.005$ m, $\gamma_2 = 3.04$ and $w_2 = 0.0036$ cm$^{4-\gamma_2} = 4.331 \times 10^{-5}$ m$^{4-\gamma_2}$, as in SAX99.

The slice of the 2D spectrum along the positive k_x-axis is shown in Fig. 26 and a 200 cm × 200 cm rough surface realization based on the above spectrum is shown in Fig. 27(a). The surface resembles sand wave ripples with a 20 cm wavelength along the x-direction and has a superimposed power-law roughness as in Eq. (4). Limited by the available workspace of our CNC milling machine, we selected a region from the simulated surface (the lower left section labeled with a red box, 60 cm × 40 cm) to make the model seafloor since it has the most pronounced ripple features. This portion of the surface is shown in detail in Fig. 27(b). While the RMS amplitude of the entire realization is 5 mm, the RMS amplitude of the surface portion to be machined is actually 7.3 mm.

The seafloor model was designed specifically to be rough, not smooth. It has a continuously varying distribution of surface heights. Hence, it was not suitable to adopt the conventional coarse and fine machining process since they do not share the same the tool path. In theory, a simple approach to create the rough surface is to use a very small spherical cutter throughout the machining process. However it would take a tremendous amount of machining time to complete the project and the cutter would likely break during the long machining process. We used a flat end-cutter to do the coarse machining. The flat end-cutter was used to *peel* off the material above the design surface layer by layer. The cutter was commanded to move at a constant height such that the full cutting edge can be used to remove maximum amount

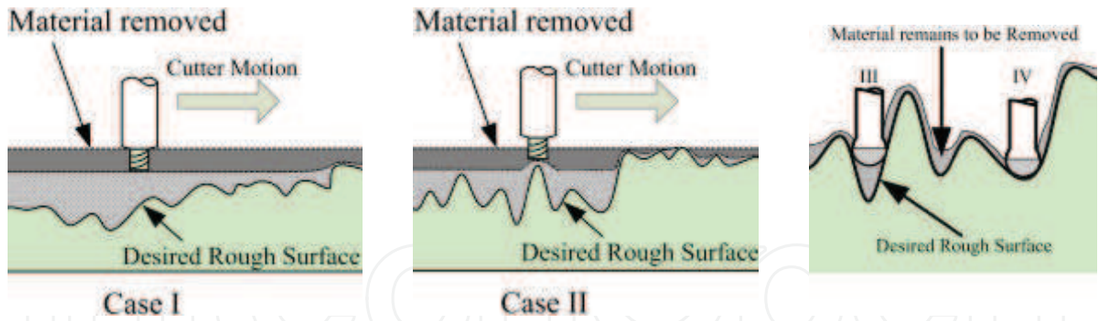

Fig. 28. (a) Coarse machining process for the rough surface. For Case I, the full cutting edge is used to remove material; for Case II, the cutter is lifted upward 1 mm to avoid overcutting the surface. (b) Fine machining process for the rough surface. For Case III, the radius of the cutter is larger than the curvature of the valley so an undercut is encountered, as opposed to Case IV where the cutter reaches the desired surface.

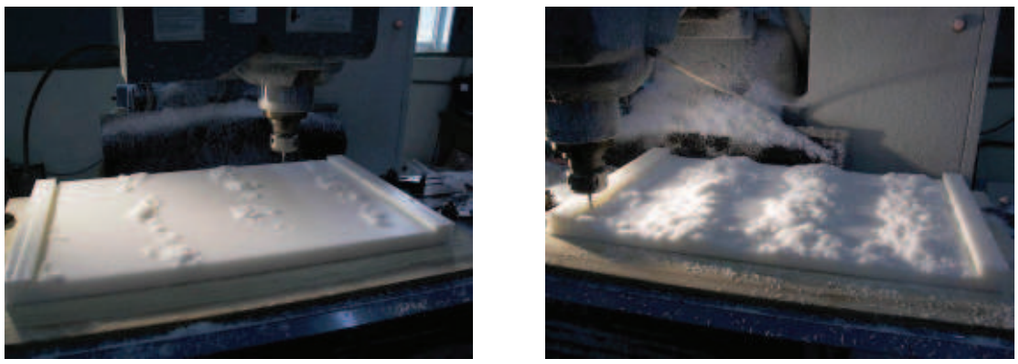

(a) (b)

Fig. 29. Coarse machining of (a) the first layer and (b) the second layer.

(a) (b)

Fig. 30. (a) Finished surface. (b) Close-up of the finished surface showing the small scale roughness features and the machining marks.

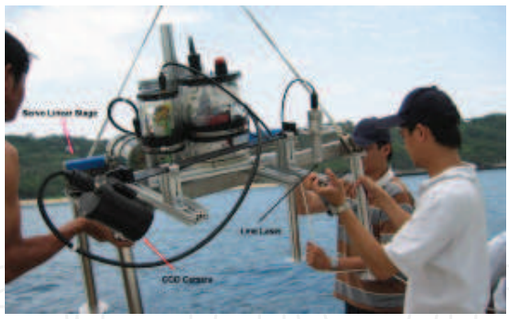

Fig. 31. IUT-NSYSU underwater laser line scanner and linear track.

of material while a one-mm clearance above the design surface was kept to preserve the material for fine machining later on. This process was repeated several times until any further feed along vertical direction would overcut the design surface. With the help of a machining simulation program, we decided to choose a ϕ 4 mm end cutter to do the coarse machining, and a ϕ 1 mm spherical cutter to do the finishing. These machining procedures are explained in Fig. 28. The model surface, corresponding to the input to the CNC milling machine, is shown in Fig. 29 and 30(a). As seen in the closeup of the finished surface shown in Fig. 30(b), the machining marks are much smaller than the relevant surface features.

5.2 Model surface measurement

The measurement is carried out by our underwater laser scanner called *Seafloor Laser Scanner* (SLS) as shown in Fig. 31. It consists of a water-proof laser line scanning head assembly and a one-meter servo linear stage. The scanning head assembly maintains the relative position and orientation between the camera and the laser source while the linear stage advances. The camera is a Basler A102f camera with a resolution 1388 $\times$ 1038 pixels CCD (charge coupled device). The wavelength of the laser is 650 nm, and a cylindrical lens is placed at its tip to generate a 60° fan angle. The scanning head assembly was kept roughly 75 cm above the model surface to have an effective scanning swath about 40 cm. The camera was tilted down to look at the laser reflection with a 30° grazing angle. The stage was commanded to profile the model surface with 2.3 mm/sec while the camera acquires about 5 to 6 images per second. With this frame rate, the scanning resolution is about 0.5 mm along track. For simplicity of the design, there is no synchronization signal between the motion of the linear stage and the camera acquisition. Assuming that the linear stage moved with constant speed, the distance relative to the first image frame along the track was estimated based on the time stamp of the image. The measured ripple surface is shown in Fig. 32(b).

5.3 Comparisons

Point-to-point comparisons of the measurement acquired by the laser scanning to the model surface is difficult because the measurement are not described in the CAD coordinate system. With that in mind, we display the surfaces with color coding of the height to have an overall idea of the similarity. We used the same color scale to plot the surfaces as shown in Fig. 32. Several features on the surface, denoted as **A** to **E**, are indicated for visual comparison. At **A**, a cross shape groove shown in the model surface is also found in the reconstructed surface. This is also the case at **B** for an isolated summit, at **C** for a kidney shape valley, at **D** for a T shape valley, and at **E** for two consecutive valleys. These similarities provide evidence that SLS works well, but the results do not provide a quantitative characterization of similarity.

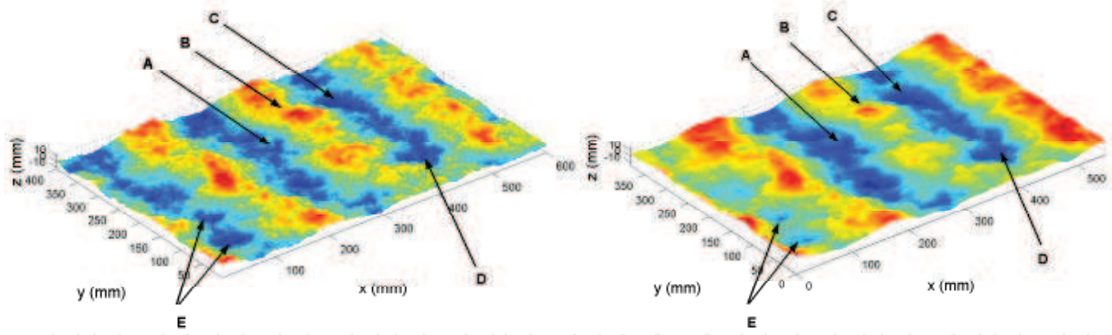

(a) (b)

Fig. 32. Reconstructed surface from (a) the CAD model and (b) the laser scan.

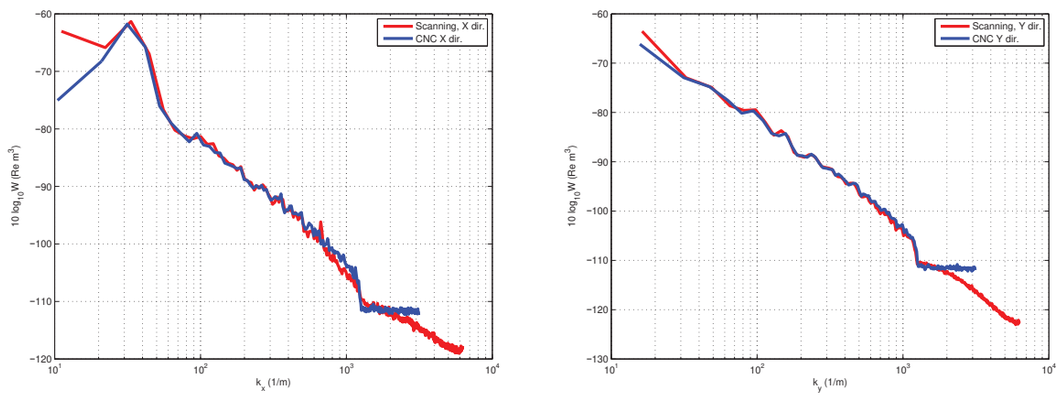

(a) (b)

Fig. 33. Comparison of the marginal spectrum (a) along the x-direction (perpendicular to the ripple crests) and (b) along the y-direction (parallel to the ripples) between CNC ripple model (blue-solid line) and laser scan (red-solid line).

While it was not possible to compare the measurement on a point-by-point basis, quantitative comparisons of the marginal spectra can be performed since they are mean 1-D spectra along the x- or y-axes. By taking the integral of the 2-D spectrum, the resulting marginal spectra are only weakly dependent on the orientation and alignment of the surface. These effects can further be mitigated by applying a 2D Hanning window to each the measurement prior to the determination of the power spectrum. This also reduces the effects of the wrap-around discontinuity of the boundary on the power spectrum of the reconstructed surface. The 1-D marginal spectra of the measurements and the model surface are shown in Fig. 33(a) and 33(b). For the marginal spectrum along the x-direction, SLS detects the existence of the ripples with the correct wavenumber and intensity. And it follows closely to the model surface spectra in the wavenumber range k_1 to k_2. The high frequency cut-off was also detected correctly. Wavenumber beyond the high frequency cut-off, SLS measurement starts to deviate from the CAD model. The RMS difference between the SLS results to the the model surface spectrum in the wavenumber range k_1 to k_2 is 1 dB in the x-direction, and 0.4 dB in the y-direction (Fig. 34). This indicates that SLS is accurately measuring the surface spectra in the wavenumber range k_1 to k_2. It should be noted that computation of the roughness spectra involves nearly two hundred thousand measurement points. It is the statistical characteristics of the large

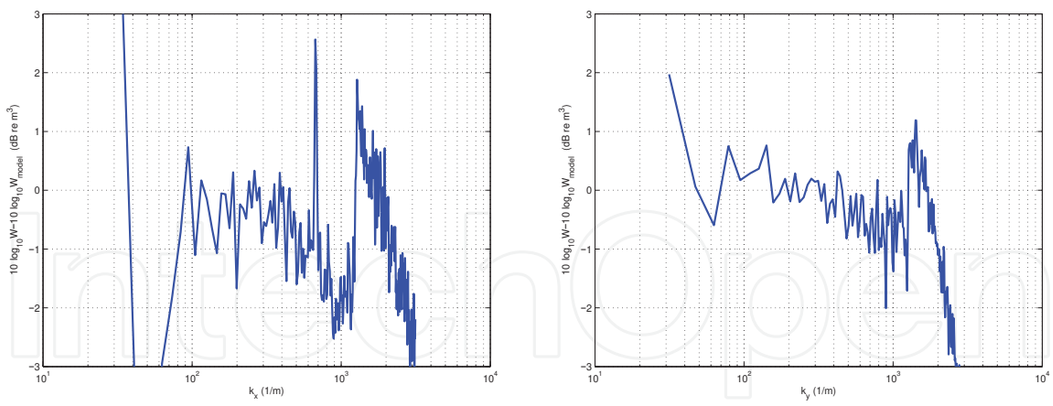

(a) (b)

Fig. 34. Difference of the marginal spectra determined from the measurement and the CAD model surface along (a) the x-direction and (b) the y-direction. The range of k in each figure is from k_1 to k_2 which are defined in Subsection 5.1.

ensemble. In other words, it is not possible to affect trend of the spectra by removing or changing a subset of the data. It is accurate or inaccurate as it is.

6. Field experiment

In the summer of 2006, the US Office of Naval Research sponsored an experiment, Shallow Water 2006 (SW06), off the New Jersey coast. SLS was mounted on an existing sediment conductivity probe (In situ Measurement of Porosity, second generation - IMP2) and deployed jointly to measure bottom roughness spectra (Tang, 2004; Wang & Tang, 2009). IMP2 has been deployed in several acoustic experiments and provides reliable 1D bottom roughness along a 4-meter-long transect with a 10-mm horizontal sample interval and 1-mm vertical resolution. Its working principle is to measure the conductivity, so the system is robust to turbidity of the water but it provide only one transect per run. The details of its specifications and performance can be found in (Tang, 2004). On the other hand, SLS is limited by the water quality but it provides both 1D and 2D roughness spectra at a much higher spatial sampling density. Integrating these two methods offers an opportunity to compare the measured spectra from both methods at the same location in the field.

6.1 Field operation and seafloor microbathymetry

The SLS scanning head assembly, mounted on the horizontal linear stage of IMP2, was kept roughly 75 cm above the seafloor to achieve an effective scanning swath of 30 cm. The CCD camera was tilted downward to face the laser reflection at a 30° grazing angle. With this configuration, the optical resolution on the scanning plane (across track) is 0.3 mm.

The integrated system was deployed on August 14 (39°01.3559′N, 73°02.2294′W) and 17 (39°01.5506′N, 73°02.7994′W), 2006, in 80-m water depth. The measurement started with the conductivity probing from the home position of the linear stage out to 4 m followed by the laser scanning during the return trip of the linear stage to its home position. SLS was normally facing forward along the motion of the linear stage of IMP2. In this configuration, the IMP2 10-cm probing marks would not be in the view of SLS. To make direct comparison between the data from IMP2 and SLS, we turned the camera axis 30° to the side to ”see” the IMP2 marks

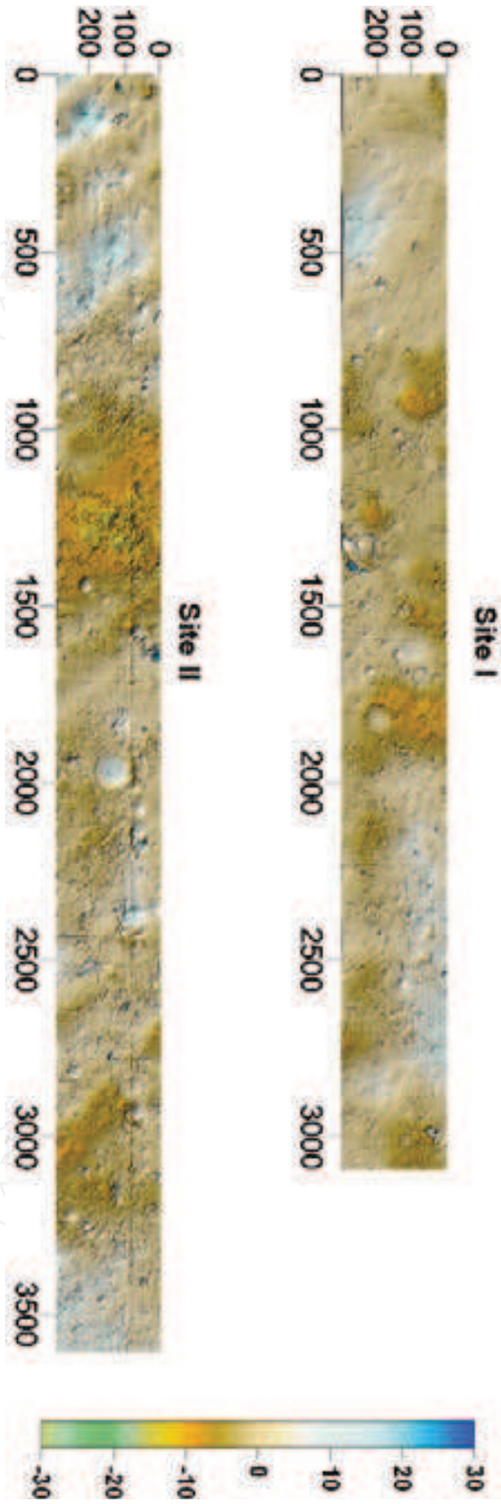

Fig. 35. SLS color-shaded relief maps for Site I and Site II. (All units are in mm). Note the IMP2 marks for Site II show as a stitch line near 100 mm on the vertical axis.

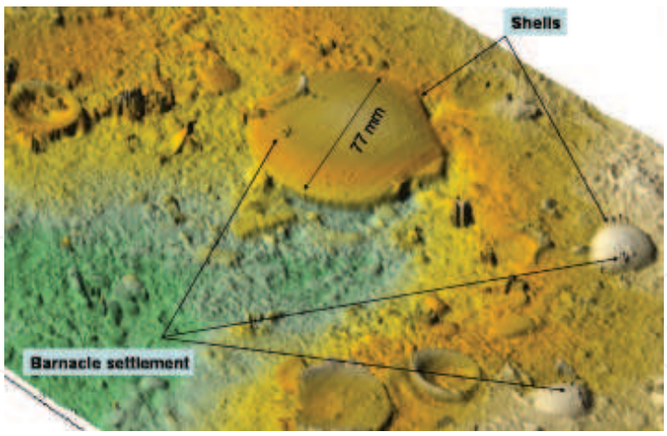

Fig. 36. A close-up view of Fig. 35 for Site I. Fine features depicted by the laser scanning: barnacle encrustations on shell surfaces.

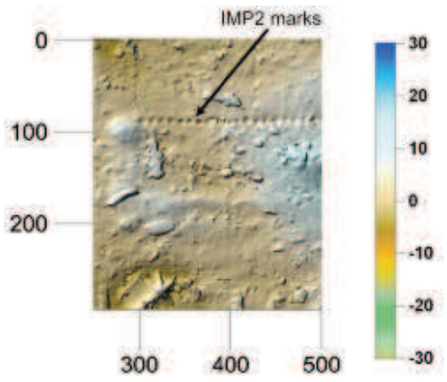

Fig. 37. A close-up view of the laser scanning that shows craters created by IMP2. The center-to-center distance between probing marks is 1 cm. (All units are in mm.)

in one of the two deployments. In either configuration, the overall area sampled is about 30 cm $\times$ 360 cm with sub-mm resolution in both vertical and horizontal directions. The sampled seafloor data points provided by these two apparatuses were roughly 400 for IMP2 and over 1,000,000 for SLS.

The rough sea bottom acquired by SLS presented in color-shaded relief maps for these two deployments are shown in Figs. 35. The shaded relief maps show that the seafloor was covered with abundant features such as shell fragments and sediment mounds and pits. Neither site shows the obvious presence of ripple fields. Site I showed no signs of disturbance by surface waves, and no apparent ripple field was found. At Site II, also full of benthic features like Site I, there were several weak crests, barely visible, lying along the upper-left to lower-right direction. According to Horikawa & Watanabe (1967), at 80 m depth, the seafloor is not influenced by the surface wave motion under normal conditions. The roughness features are most likely due to bottom currents and biological activities. The SLS's ability to portray the details of the features on the seafloor is demonstrated by a close-up of the SLS image from the first site (Fig. 36). Barnacle encrusting the surface of three shells are clearly visible in the figure. The dimension of the encrustations is 1 - 2 millimeters. Probing marks made during IMP2 measurements on the seafloor are also visible as a "stitch line" for Site II in Fig. 35. Center-to-center distance between the marks was 1 cm, which was the sampling

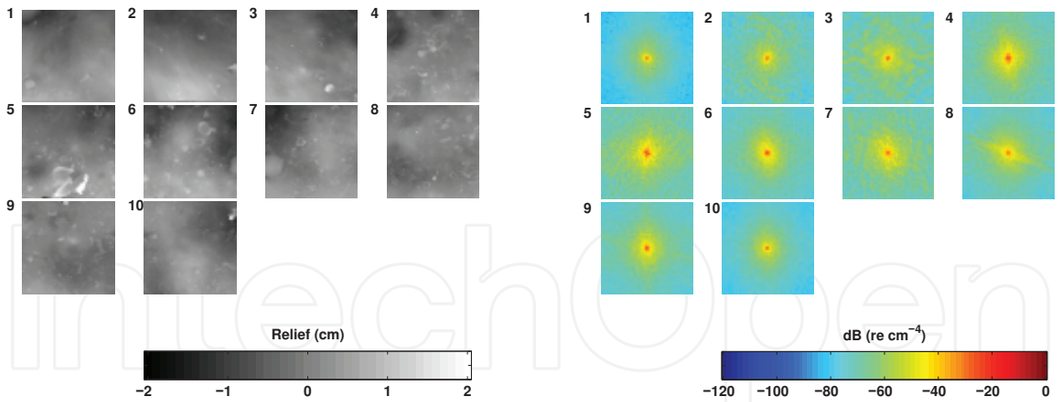

Fig. 38. Subdivided relief patches on the left and their 2D Spectra on the right for Site I. The size of the patch is 30 cm $\times$ 30 cm, and the wavenumbers k_x and k_y on the 2D spectra plots are from -31.5 (rad/cm) to to 31.5 (rad/cm) in linear scale. The number on the upper left corner of each relief map represents its sequence from left to right with respect to the original large map. The corresponding 2D spectrum is given with the same number on the right panel.

interval of IMP2. With a close-up look of the line as shown in Fig. 37, when the IMP2 probe was lowered into the sediment, it created a small pit with a diameter about 4 mm. As the probe retrieved, the sediment around the probe was piled up to form a mound around the pit like a crater. Individual 'stitch mark' was about 8 to 9 mm in diameter and a couple of millimeters in height. These marks make point-to-point comparison between the IMP2 and the SLS measurement impossible. However, the comparisons can be made on roughness spectra level.

6.2 Roughness spectrum

The area scanned by SLS is a slender rectangle, roughly 360 cm long and 30 cm wide. For the 2D spectral analysis, we divided the rectangle into 30-cm $\times$ 30-cm patches for Site I, and 26.4-cm $\times$ 26.4-cm for Site II; no overlap was taken between patches. A 2D Hanning tapering window was applied to each of the square patches to reduce spectral leakage. The relief maps of the square patches and their corresponding 2D spectra for Site I are shown in Fig. 38 as examples. The overall roughness intensity from patch to patch were about the same except for patch No. 1. On this patch, for wavenumbers greater than 20 rad/cm, the intensity is lower by 20 dB than the other patches. On its relief map, there are less shell fragments than the other patches. Patch No. 5 has brighter intensity than others. On the corresponding relief map, much more shell fragments with irregular shapes were found than the other patches. The averaged 2D spectra of the two sites show no apparent anisotropy, but there is a substantial difference in spectral level between the them (Fig. 39). In summary, no ripple field is observed at either site, and both sites show isotropic roughness spectra. To make roughness spectra comparisons between IMP2 and SLS, we use full-length, along-track SLS data. A 1D Hanning window is applied to the IMP2 roughness profiles before estimating their roughness spectra. IMP2 only provided one realization for each site, whereas the SLS yielded multiple transects. First, we compare the SLS spectrum using only those data neighboring the IMP2 transects. A 1-cm-wide stripe which covers the IMP2 probing marks is defined as the IMP2 probing zone where the seafloor was disturbed by the IMP2 probe. Two 1.5-cm-wide stripes that are 1.5 cm away from either side of the probing zone were selected. As shown in Fig. 40,

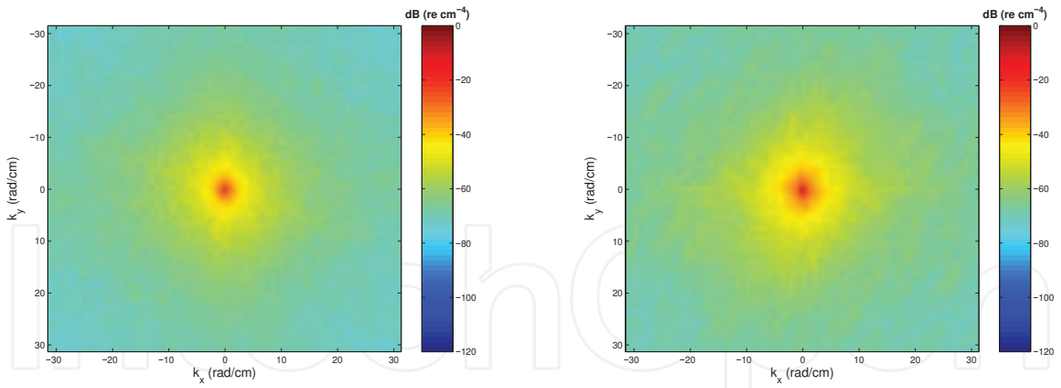

Fig. 39. Average 2D spectrum for Site I (left) and Site II (right).

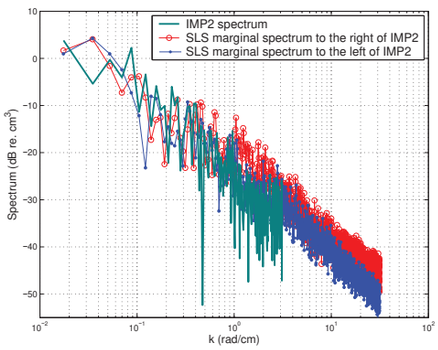

Fig. 40. Spectral comparison between data from IMP2 and data from its neighboring areas imaged with SLS.

the IMP2 spectrum agrees well with that of its left neighbor by SLS but is slightly different from that of its right neighbor for the overlapping wavenumbers. This comparison of spectra indicates that Site II roughness is variable on a small scale (centimeters). Because the SLS spectrum is a result of averaging over all transects across the 30-cm width, it is expected to be much smoother and having less statistical uncertainty than IMP2 (Figs. 41). In the figure, the IMP2 spectrum varies about the mean of the SLS spectrum for Site I; but for Site II the two measurements show visible difference for wavenumbers greater than 1 rad/cm. As discussed previously, the spectral difference is likely due to the small-scale spatial heterogeneity of the roughness. Spatial heterogeneity of bottom roughness is a major concern for modeling acoustic backscatter. The observed heterogeneity suggests that closely spaced multiple areas need to be scanned in order to get statistically representative estimates of the roughness.

The SLS's ability to detect minute roughness spectral components on the seafloor is shown in Fig. 42 as a close-up view of the Site II spectrum. A prominent spectral peak exists at wavenumber K=6.028 rad/cm, or spatial wavelength λ=1.033 cm, close to the sampling interval of 1 cm that IMP2 was configured. Also shown for comparison is the spectrum calculated from data excluding those from the IMP2 probing zone, and this spectrum does not have the spectral peak. The probing zone occupied about 3% of the totally scanning area. In other words, SLS in very keen on detecting the minute change of the seafloor.

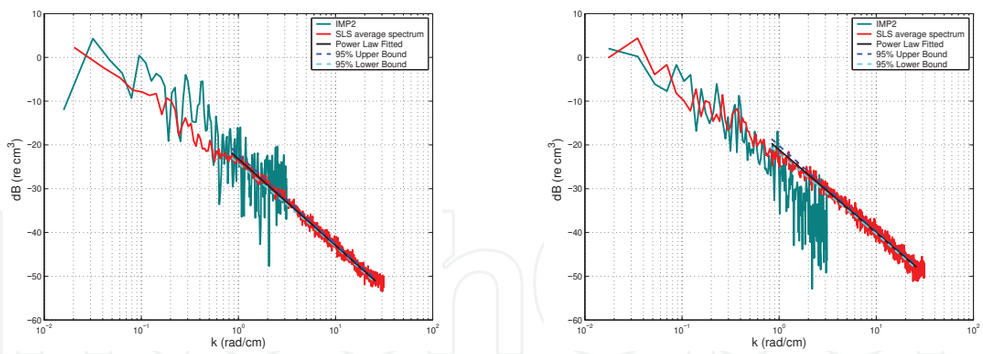

(a) Site I (b) Site II

Fig. 41. Spectral comparison between IMP2 and SLS (the average of the 1-cm-wide stripes of the scanned area).

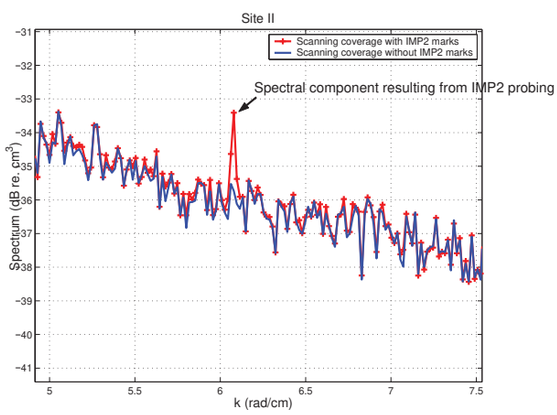

Fig. 42. Spectral component resulting from the IMP2 probing marks. (IMP2 sampling interval 1 cm is equivalent to wavenumber 6.28 rad/cm.)

7. Summary

We present a convenient method for calibrating the CCD camera used in an underwater laser scanning system, Seafloor Laser Scanner. We let the CCD camera capture the image of a calibration board on which grid points of equal span are laid. Longitude and latitude lines obtained with curve-fitting of the grid points are used to infer the world coordinates of target points. Because the method only uses a board for implementing the calibration scheme, it is easier than other approaches that need a rigid control frame. Only one image of the calibration board is needed, and it can be done before or after the measurement as long as the scanning head is not disassembled yet. Both on-plane measurement and laser scan line profiling give results with percentage error less than 1%. A simulated sandwave model test piece fabricated with CNC milling machine is scanned in the lab tank. The data points are adjusted to reconstruct the surface of a model sandwave. Because the mathematical equation of the sandwave is known, we compare the measurement results with the theoretical values at specific locations. The experiment shows that our approach can measure sandwave of amplitude as small as 2. mm from one meter away with error bound less than 1.5 mm.

Our ultimate goal is to use SLS to obtain the 2D roughness spectrum of seafloor, which is an important boundary condition for modeling high frequency acoustic scattering problem. Therefore, we fabricated a roughness-known surface model to evaluate the performance of SLS in measuring rough spectra. Our target spectrum, inheriting the characteristics of the seafloor at the SAX99 experiment site, consists of the superposition of a shifted Gaussian spectrum and an isotropic power law spectrum. The former generates ripples along the dominant direction and the latter produces fine scale rough features on the surface. A multi-stage CNC machining strategy, coarse machining and fine machining, was used to fabricate this model surface. In coarse machining, a large end-cutter is used to remove the relief depth down to a thin layer of clearance above the final desired surface. In fine machining, a small spherical cutter with dense tool paths was used to remove the remaining material to create the desired surface. Surface data measured by SLS were converted to marginal spectra parallel and perpendicular to the ripples, and compared to that of the model surface to assess its performance. SLS measured the model surface spectrum up to $k = 1256.6/m$ with an RMS error of less than 1 dB. The results of these assessments provide a means to set the reliable bounds for the roughness spectrum measurement of SLS. This surface is a useful tool for the evaluation of optically-based roughness measurements in both a laboratory setting and for *in situ* measurements.

SLS was designed to be compact and self-contained such that it can be mounted on IMP2 as an add-on module. This integrated system was deployed to acquire data on fine-scale seafloor roughness during the Shallow Water 2006 Experiment. The 3D bathymetry provided by the laser scanner revealed a seafloor full of shell hash. The effectiveness of the laser scanner for imaging the details of the seafloor was demonstrated by discerning fine features such as barnacles encrusting the surface of shells and small probing marks left by IMP2 in the imagery. The microbathymetry of the seafloor was divided into small patches, and the corresponding 2D spectra were estimated. No evidence of ripple fields was found and the seafloor roughness spectra were found to be azimuthally isotropic. The 1D spectra calculated from microbathymetry obtained by IMP2 and the laser scanner were compared over the same wavenumbers and exact locations. Individual 1D spectral lines from SLS, when compared with the IMP2 spectra, show good agreement at Site I, but different by several decibels at site II due to small-scale variability. Approximately a 4 dB difference was found in roughness spectral level between the two SW06 sites 900 m apart. A study of spatial heterogeneity of bottom roughness would benefit greatly by data that cover significantly greater areas of seafloor than so far attempted. One possibility is to mount an imaging system on a moving platform such as an AUV.

8. Acknowledge

This work was supported in part by National Science Council of Taiwan through contract NSC92-2611-E-110-005, and in part by the Asian Pacific Ocean Research Center, National Sun Yat-sen University. Field trials were supported by the Office of Naval Research Ocean Acoustics Program. We thank Min-Shine Chen, Po-Chi Chen and Min-Wei Hung at the Institute of Undersea Technology, Sun Yat-sen University for their technical contributions, and APL's technical staff for the deployment support.

9. References

Briggs, K. B. (1989). Microtopographical roughness of shallow-water continental shelves, *IEEE Journal of Oceanic Engineering*. 14: 360–367.

Briggs, K. B., Tang, D. & Williams, K. L. (2004). Characterization of interface roughness of rippled sand off Fort Walton Beach, Florida, *IEEE J. Oceanic Eng.* 29(4): 505–514.

Broadwater, J. (1988). Supporting Underwater Archeology with Ocean Technology, *OCEANS '88*, pp. 837 – 839.

Campbell, J. B. (2006). *Introduction to remote sensing*, 4th edition, edn, Guildford Press, New York.

Chen, C. & Kak, A. (1989). Modeling and calibration of a structured light scanner for 3-D robot vision, *Proceedings of 1987 International Conference on Robotics and Automation*, Vol. 4, pp. 807–815.

Crawford, A. & Hay, A. (1998). A Simple System for Laser-Illuminated Video Imaging of Sediment Suspension and Bed Topography, *IEEE Journal of Oceanic Engineering* 23(1): 12–19.

Gujarati, D. (2003). *Basic Econometrics*, McGraw-Hill, New York.

Horikawa, K. & Watanabe, A. (1967). A study on sand movement due to wave action, *Coastal Eng. in Japan* 10: 39–57.

Klimley, A. & Brown, S. (1983). Stereophotography for Field Biologist: Measurement of Length and Three Dimensional Positions of Free Swimming Sharks, *Marine Biology* pp. 175–185.

Kocak, D., Caimi, F., Das, P. & Karson, J. (1999). A 3-D Laser Line Scanner for Outcrop Scale Studies of Seafloor Features, *Proc. of MTS/IEEE Oceans '99*, Vol. 3, pp. 1105–1114.

K.S. Fu, R. G. & Lee, C. (1987). *Robotics: Control, Sensing, Vision and Intelligence*, McGRAW Hill, New York.

Kuga, Y. & Phu, P. (1996). Experimental studies of millimeter-wave scattering in discrete random media and from random surfaces, *Prog. Electromag. Res. (PIER)* 14: 37–88.

Li, Y., Young, T. & Huang, C. (1989). Noncontact Measurement Using Line-Scan Cameras: Analysis of Positioning Error, *IEEE Transactions on Industrial Electronics* 36(4): 545–551.

Mellema, G. R. (1999). *Subcritical acoustic scattering across a rough fluid-solid interface*, PhD thesis, Department of Electrical Engineering, University of Washington.

Melling, A. (1997). Tracer particles and seeding for particle image velocimetry, *Measurement Science and Technology* 8(12): 1406–1416.

Myers, W. (1980). Industry Begins to Use Visual Pattern Recognition, *Computer* 13(5): 21–31.

Ogawa, Y. (2000). Image Processing for Wet Welding in Turbid Condition, *Proc. of the 2000 International Symposium on Underwater Technology*, Tokyo, Japan, pp. 457–462.

Raffel, M., Willert, C., Wereley, S. & Kompenhans, J. (2007). *Particle Image Velocimetry: A Practical Guide (Experimental Fluid Mechanics)*, 2nd edition, edn, Springer, Berlin.

Rocher, L. & Keissling, A. (1975). Methods for Analyzing Three-Dimensional Scenes, *Proc. 4th Intl. Joint Conf. Artificial Intelligence*, pp. 669–673.

Son, S. & Lee, K. H. (2002). Automated laser scanning system for reverse engineering and inspection, *International Journal of Machine Tools & Manufacture* 42: 889–897.

Summers, J. E., Soukup, R. J. & Gragg, R. F. (2005). Characterization and fabrication of synthetic rough surfaces for acoustical scale-model experiments, *Technical report*, Naval Research Laboratory, Code 7140.

Tang, D. (2004). Fine-scale measurements of sediment roughness and subbottom variability, *IEEE J. Oceanic Eng.* 29(4): 929–939.

Thorsos, E. I., Williams, K. L., Chotiros, N. P., Christoff, J. T., Commander, K. W., Greenlaw, C. F., Holliday, D. V., Jackson, D. R., Lopes, J. L., McGehee, D. E., Richardson, M. D., Piper, J. E. & Tang, D. (2001). An overview of SAX99: Acoustic measurements, *IEEE Journal of Oceanic Engineering.* 26: 4–25.

Thorsos, E. I., Williams, K. L., Jackson, D. R. & Tang, D. (2000). High-frequency sound interaction in ocean sediments, *in* M. Zakharia, P. Chevret & P. Dubail (eds), *Proceedings of the fifth European Conference on Underwater Acoustics*, Vol. 1, Office for Official Publications of the European Communities, Luxemburg, pp. 275–280.

Wang, C. C. & Cheng, M. S. (2007). Nonmetric camera calibration for underwater laser scanning system, *IEEE Journal of Oceanic Engineering.* 32: 383–399.

Wang, C. C. & Tang, D. (2009). Seafloor roughness measured by a laser line scanner and a conductivity probe, *IEEE Journal of Oceanic Engineering.* 34: 459–465.

Williams, K. L., Jackson, D. R., Thorsos, E. I., Tang, D. & Briggs, K. B. (2004). Acoustic backscattering experiments in a well characterized sand sediment: Data/model comparisons using sediment fluid and Biot models, *IEEE Journal of Oceanic Engineering.* 29(4): 412–428.

Laser Scanning, Theory and Applications
Edited by Prof. Chau-Chang Wang

ISBN 978-953-307-205-0
Hard cover, 566 pages
Publisher InTech
Published online 26, April, 2011
Published in print edition April, 2011

Ever since the invention of laser by Schawlow and Townes in 1958, various innovative ideas of laser-based applications emerge very year. At the same time, scientists and engineers keep on improving laser's power density, size, and cost which patch up the gap between theories and implementations. More importantly, our everyday life is changed and influenced by lasers even though we may not be fully aware of its existence. For example, it is there in cross-continent phone calls, price tag scanning in supermarkets, pointers in the classrooms, printers in the offices, accurate metal cutting in machine shops, etc. In this volume, we focus the recent developments related to laser scanning, a very powerful technique used in features detection and measurement. We invited researchers who do fundamental works in laser scanning theories or apply the principles of laser scanning to tackle problems encountered in medicine, geodesic survey, biology and archaeology. Twenty-eight chapters contributed by authors around the world to constitute this comprehensive book.

INTECH
open science | open minds

InTech Europe
University Campus STeP Ri
Slavka Krautzeka 83/A
51000 Rijeka, Croatia
Phone: +385 (51) 770 447
Fax: +385 (51) 686 166
www.intechopen.com

InTech China
Unit 405, Office Block, Hotel Equatorial Shanghai
No.65, Yan An Road (West), Shanghai, 200040, China
中国上海市延安西路65号上海国际贵都大饭店办公楼405单元
Phone: +86-21-62489820
Fax: +86-21-62489821

IntechOpen